NANO LETTERS

pubs.acs.org/NanoLett Letter

Single Nanoparticle Collision Electrocatalysis Driven by Ultrafast High-Temperature Precision Synthesis

Lixia Yang, Yuanhua Tu, Xiangyi Shan, Pengfei Wang, Jianan Xu, Han Gao, Furong Cai, Zhiming Cui, Zhaoyu Jin, and Min Zhou*

Cite This: *Nano Lett.* 2025, 25, 8320−8326

Read Online

ACCESS | Metrics & More | Article Recommendations | Supporting Information

ABSTRACT: The single nanoparticle (NP) collision strategy offers a promising alternative to traditional ensemble methods in electrocatalysis, providing unique insights into catalytic behavior that cannot be captured by ensemble-based techniques. However, synthesizing colloidal NP catalysts with tunable composition, uniform size, and near-pristine surfaces remains a significant challenge. Here, using Pt_xRu_{1-x} alloys as a model system, we propose an innovative strategy that combines ultrafast high-temperature precision synthesis with ultrasonic exfoliation. This approach enables the preparation of colloidal catalysts with the desired properties, which were previously difficult to achieve. Single NP collision electrocatalysis uncovers the composition-dependent intrinsic activity of the methanol oxidation reaction (MOR) at industrial current densities, bypassing mass transfer limitations. Density functional theory (DFT) calculations highlight the Pt−Ru synergistic effect in optimizing MOR performance. This study, for the first time, integrates ultrafast precision synthesis with single NP electrocatalysis, providing a new framework for the development of highly efficient catalysts.

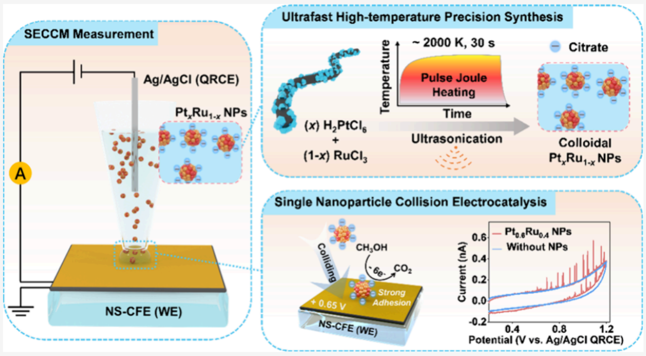

KEYWORDS: *Ultrafast precision synthesis, Colloidal catalyst, Single nanoparticle collision, Intrinsic activity*

The performance of catalysts is crucial in energy conversion and storage.[1] Traditional research methods often focus on catalyst nanoparticle (NP) ensembles, but they struggle to accurately reflect the real catalytic behavior of single NPs.[2] Due to macroscopic effects and mass transfer limitations, these methods inherently struggle to precisely evaluate catalytic performance.[3,4] Therefore, studying the catalytic behavior of single NPs can provide more accurate guidance for catalyst design and optimization.[5−9]

The single NP collision technique offers a new approach for uncovering the essence of catalytic reactions, enabling real-time monitoring and precise measurement of the catalytic activity and kinetic properties of single NPs.[2−7] This technique requires extremely high standards for the size, composition, and surface cleanliness of NPs, demanding uniformity across samples.[6,7] However, conventional colloidal synthesis methods often rely on long-chain stabilizers,[10,11] which, although they can regulate NP properties, obscure active sites and limit their application in single NP collision electrocatalysis. Despite nearly two decades of development in single NP collision electrocatalysis,[12,13] research materials are still predominantly focused on a few metals (e.g., Ag, Au, Pt) and metal oxides (e.g., RuO_x and IrO_x) protected by loosely capped, short-chain citrates.[14] Therefore, there is an urgent need to develop an efficient, colloidal NP preparation method that yields near-pristine surfaces (citrate capped),[14] high monodispersity, and tunable composition, to advance the application and development of this technique.

In recent years, advanced ultrafast high-temperature synthesis techniques have provided innovative pathways for large-scale NP materials preparation,[15] which are able to regulate the composition of the particles while ensuring a consistent particle size. Coupled with high-resolution characterization techniques, these methods have provided reliable support for studying the composition−structure−performance relationships of nanocatalysts.[15,16] These techniques have significantly expanded the range of single-metal species and multimetallic element combinations and ratios that can be synthesized, creating an unprecedentedly vast nanomaterials library.[17,18] To date, studies converting metal NPs synthesized by such techniques into colloidal NPs with near-pristine surfaces, high monodispersity, and tunable composition through ultrasonic exfoliation have not been reported. Scanning

Received: March 8, 2025
Revised: May 6, 2025
Accepted: May 7, 2025
Published: May 9, 2025

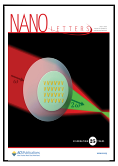

https://doi.org/10.1021/acs.nanolett.5c01519

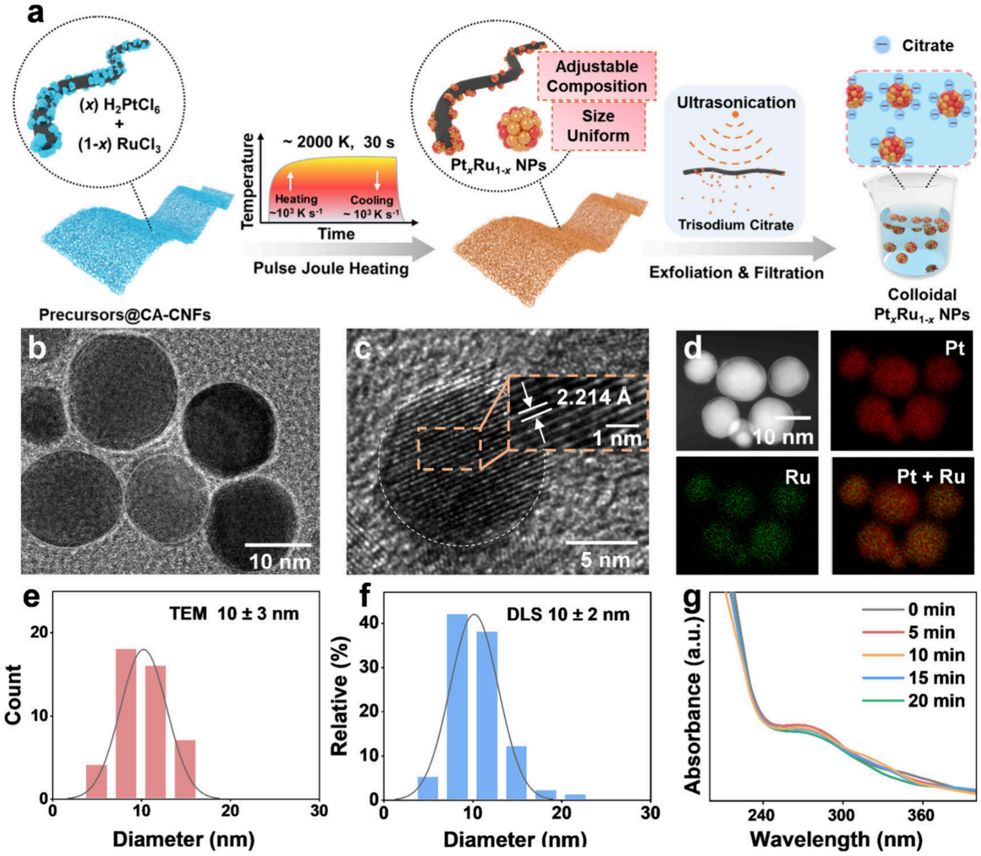

Figure 1. Preparation and characterization of colloidal Pt$_x$Ru$_{1-x}$ NPs. (a) Schematic of colloidal NP synthesis: metal salt precursors are loaded onto CA-CNFs, followed by pulse Joule heating and ultrasonic exfoliation to generate monodispersed colloidal Pt$_x$Ru$_{1-x}$ NPs. (b, c) TEM and HAADF-STEM images of colloidal Pt$_{0.6}$Ru$_{0.4}$ NPs. (d) EDS elemental mapping of colloidal Pt$_{0.6}$Ru$_{0.4}$ NPs. (e, f) Size distributions of colloidal Pt$_{0.6}$Ru$_{0.4}$ NPs determined by TEM (the source of the TEM statistical graph is shown in Figure S9a−d) and DLS. (g) UV−vis spectroscopy showing the temporal stability of colloidal Pt$_{0.6}$Ru$_{0.4}$ NPs.

electrochemical cell microscopy (SECCM) is an effective technique in the field of electrocatalysis, with low background and high spatiotemporal resolution, enabling high-resolution measurements of the electrochemical properties of NPs at the single-particle level, providing insights into local environments and reaction dynamics that cannot be obtained with traditional methods and providing a unique platform for studying the intrinsic activity of individual NPs.[19,20]

In this context, we propose an innovative strategy that combines ultrafast high-temperature precision synthesis with ultrasonic exfoliation, using Pt$_x$Ru$_{1-x}$ as a model system. This approach enables the rapid preparation of colloidal NPs with desired properties that were previously difficult to achieve. By integrating single NP collision electrocatalysis with density functional theory (DFT) calculations, we systematically elucidate the relationship and underlying mechanisms between composition and activity at the single NP level.

Figure 1a shows the preparation process of colloidal Pt$_x$Ru$_{1-x}$ NPs. Metal salt precursors were loaded onto CO$_2$-activated carbon nanofibers (CA-CNFs) in proportion, followed by pulse Joule heating to form high-density, monodispersed NPs@CA-CNFs. Ultrasonic exfoliation and filtration then produced colloidal NPs with nearly exposed surfaces, citrate-capped. CA-CNFs with high-density defects exhibited excellent precursor-loading capacity (Figures S1 and S2). Using pulse Joule heating (Figure S3), nine types of Pt$_x$Ru$_{1-x}$ NPs@CA-CNFs were synthesized (Figures S4 and S5). Inductively coupled plasma optical emission spectroscopy (ICP-OES) confirmed that the elemental molar ratio matched the feeding amounts for Pt$_x$Ru$_{1-x}$ NPs@CA-CNFs (Table S1). Additionally, X-ray photoelectron spectroscopy (XPS; Figure S6) analysis of Pt$_{0.7}$Ru$_{0.3}$ NPs@CA-CNFs, Pt$_{0.6}$Ru$_{0.4}$ NPs@CA-CNFs, and Pt$_{0.5}$Ru$_{0.5}$ NPs@CA-CNFs further verified that the surface elemental molar ratios of the catalysts are consistent with the ICP-OES results (Table S2), indicating that the surface composition of the catalysts is identical to their bulk composition. X-ray diffraction (XRD) patterns (Figure S7) showed that the Pt$_x$Ru$_{1-x}$ NPs@CA-CNFs maintained a face-centered-cubic (FCC) structure with no phase separation observed, while high-resolution transmission electron microscopy (HRTEM) images (Figure S8) revealed the (111) plane as the dominant facet at both the particle edge and center. Overall, such characterizations confirm that the synthesis method effectively produced Pt$_x$Ru$_{1-x}$ NPs@CA-CNFs with uniform size and tunable composition, with exposed surface facets that align with the bulk facets.

The preparation of stable monodispersed colloidal NPs is a prerequisite for evaluating the electrocatalytic performance of Pt$_x$Ru$_{1-xx}$ NPs. Colloidal Pt$_{0.6}$Ru$_{0.4}$ NPs were characterized as a representative sample. Transmission electron microscope (TEM; Figure 1b) and scanning electron microscope (SEM; Figure S9) images showed that Pt$_{0.6}$Ru$_{0.4}$ NPs were spherical, uniformly sized, and free of carbon fiber fragments. The HRTEM image (Figure 1c) also revealed a dominant (111)

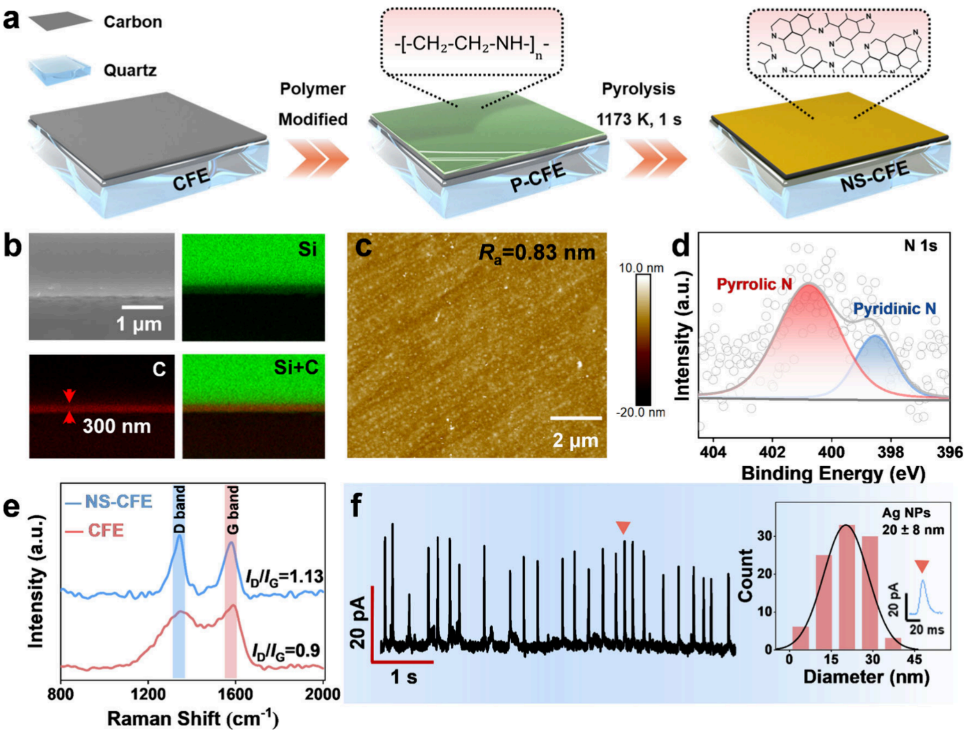

Figure 2. Interface design and characterization of the analytical electrode. (a) Schematic of the preparation of NS-CFE. (b, c) SEM and AFM images of NS-CFE. (d) XPS N 1s spectrum of NS-CFE. (e) Comparison of Raman spectra between CFE and NS-CFE. (f) Oxidative transient signals of Ag NPs colliding with NS-CFE and their size distribution; the inset shows a representative current transient.

crystal plane, revealing that the dominant crystal plane of the NPs was retained after ultrasonic exfoliation. The energy-dispersive X-ray spectroscopy (EDS) elemental mapping confirmed the uniform distribution of Pt and Ru, with the elemental molar ratio matching the feedstock (Figures 1d and S10). EDS line scan analysis (Figure S11a and S11b) further indicates that the molar ratio of elements in both the surface and bulk phases is in agreement with the feedstock ratio (Figure S11c), with no significant segregation observed. SEM (Figure S9), TEM (Figure 1e), and dynamic light scattering (DLS; Figure 1f) measurements indicated consistent NP sizes in both solid and liquid phases, matching the size of $Pt_{0.6}Ru_{0.4}$ NPs@CA-CNFs. Ultraviolet−visible (UV−vis) spectroscopy (Figure 1g) demonstrated good stability of the colloidal $Pt_{0.6}Ru_{0.4}$ NPs. These characterizations confirm the successful synthesis of colloidal Pt_xRu_{1-xx} NPs with uniform shape, size, and consistent exposure of crystal facets, making them suitable for subsequent single-particle collision electrocatalysis.

The chemical inertness of analytical electrodes and their adhesion to individual NPs are crucial for efficient single NP analysis.[21] To address these challenges, we developed a nitrogen-skinned carbon film electrode (NS-CFE). Figure 2a shows the preparation process: CFE[22] was electrochemically modified with polyethylenimine via cyclic voltammetry (CV; Figure S12a), then pyrolyzed at 1173 K to form NS-CFE.[23] A cross-sectional SEM image (Figure 2b) showed a 300 nm carbon layer, while an atomic force microscopy (AFM) image (Figure 2c) revealed surface roughness of less than 1 nm, confirming NS-CFE's adequate thickness and smoothness. XPS (Figure 2d) showed peaks at 398 eV (pyridinic-N) and 401 eV (pyrrolic-N), confirming nitrogen incorporation. Raman spectroscopy (Figure 2e) reveals a higher I_D/I_G ratio for NS-CFE, indicating increased carbon defects due to nitrogen doping.[23] In a collision experiment with 20 nm Ag NPs, NS-CFE detected numerous oxidative transients (Figure 2f), while no signals were observed without Ag NPs (Figure S12b). In contrast, CFE detected only low-frequency signals (Figure S12c). The average Ag NP sizes on NS-CFE and CFE were 20 ± 8 nm and 12 ± 4 nm, respectively, based on integrated charge.[24] The size measured on NS-CFE aligns with TEM results (Figure S12d), while the smaller size on CFE likely reflects weak adhesion, causing elastic collisions. These findings confirm that NS-CFE improves Ag NP adhesion, enabling complete oxidation of single colliding NPs.

Colloidal Pt_xRu_{1-x} NPs and highly adhesive NS-CFE were prepared, and their electrocatalytic activity for the methanol oxidation reaction (MOR) was studied using SECCM as a function of composition (Figures 3a and S13). The method employed a functionalized macro-electrode interface with high bandwidth, low noise, and sufficient mass transfer for individual NPs (under kinetic control). Strong adhesion between NPs and NS-CFE eliminated elastic collisions and electrical contact resistance. Figure 3b shows a high-sampling CV of $Pt_{0.6}Ru_{0.4}$ NPs colliding with NS-CFE, revealing transient MOR signals at high potentials, indicating the "switch-on" and "switch-off" processes.[5] The small active area of single NPs causes the MOR onset potential to be higher than that of bulk materials. Single NP collisions with different compositions were evaluated using $i-t$ curves at the same potential. Figures 3c−e show MOR current events and statistical data (peak current and integrated charge distributions) for Ru, Pt, and $Pt_{0.6}Ru_{0.4}$ single NPs, with results for other compositions in Figure S14. Transient signals were recorded at a 100 kHz sampling rate with 1 kHz low-pass filtering (time resolution ∼ 1 ms). Statistical analysis (Figure S15) showed transient durations exceed 10 ms, ensuring

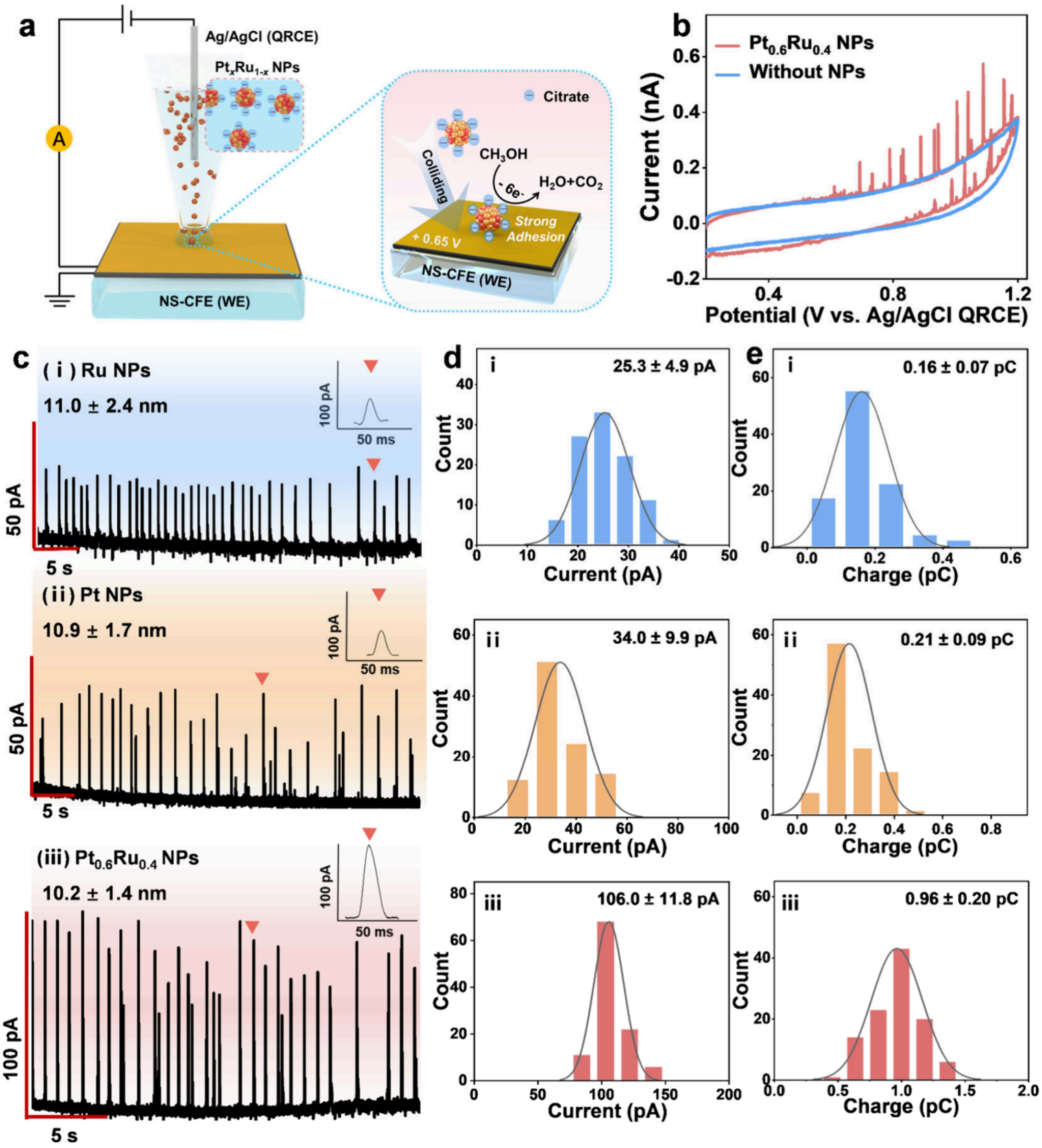

Figure 3. MOR measurements of Pt_xRu_{1-x} single NPs. (a) Schematic of the MOR for Pt_xRu_{1-x} single NPs colliding with NS-CFE based on SECCM. (b) Typical high-sampling CV of $Pt_{0.6}Ru_{0.4}$ single NP collisions, compared with the control experiment without NPs. (c−e) i−t curves, typical current events, and statistical distributions of peak current and integrated charge for Ru, Pt, and $Pt_{0.6}Ru_{0.4}$ single NP collisions.

accurate peak current measurements, with distribution matching that of catalytic activity (as discussed later). Integrated charge, being less time-resolution-dependent, is better suited for quantifying transient signals. Control experiments (Figure S16) showed no current events without methanol or NPs. CA-CNFs were also used as a control experiment to show that CA-CNFs had no interference with the collision signal of colloidal Pt_xRu_{1-x} NPs (Figure S17). Despite strong adhesion, current pulses may arise from surface poisoning or NP detachment. A single Ru or Pt NP was deposited onto carbon nanoelectrodes (Ru/Pt NP@CNE) and tested with ferrocene methanol oxidation (Figures S18 and S19), confirming that deactivation was resulting from surface poisoning, while electrical connection between NPs and CNE remained intact.

The traditional methods for measuring ensemble NPs are limited by mass transfer rates, making it difficult to accurately quantify intrinsic electrocatalytic activity. To address this challenge, we leveraged the high mass transfer properties of single NPs, enabling precise evaluation of the activities of NPs with different compositions (Figure 4a). Additionally, the smooth surface of single NPs, achieved through ultrahigh-temperature synthesis, allows their microscopic area to be approximated as the geometric surface area. This feature provides a reliable foundation for accurate activity assessment. The real current density (j_{real}) and turnover frequency (TOF) of nine Pt_xRu_{1-x} single NPs for MOR (calculation details in the methods) showed that catalytic activity increases and then decreases with Ru content, and $Pt_{0.7}Ru_{0.3}$, $Pt_{0.6}Ru_{0.4}$, and $Pt_{0.5}Ru_{0.5}$ exhibited the best performance. DFT calculations reveal Pt−Ru synergistic effects on MOR activity and intermediate adsorption Surface models of Pt−Ru alloys with varying Ru ratios were generated (Figure S20), and the most stable surfaces were selected for adsorption energy and electronic structure analysis (Figures 4b and S21, S22). CO and OH adsorption energies indicate MOR activity; high-

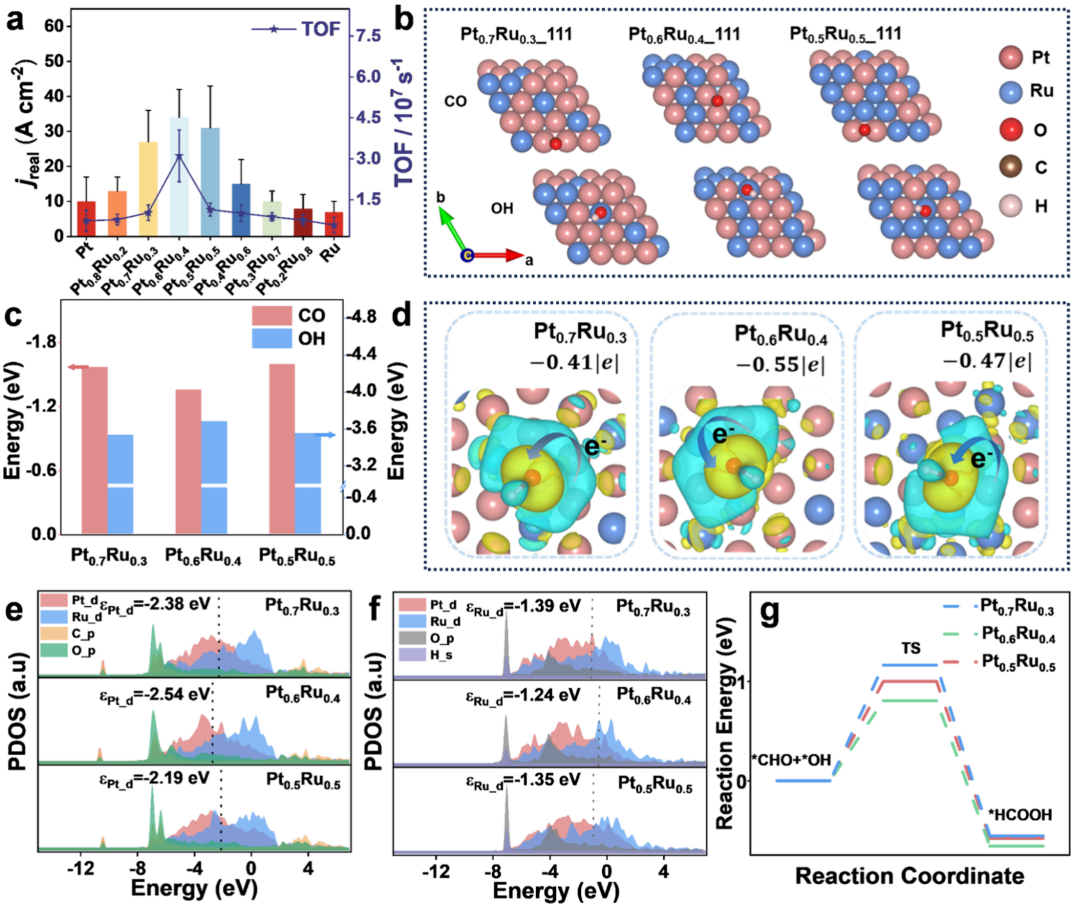

Figure 4. Composition-related MOR intrinsic activity and DFT calculations. (a) Real current density (j_{real}) and turnover frequency (TOF) on Pt_xRu_{1-x} single NPs for MOR. (b) Adsorption configurations of CO and OH on the surfaces of $Pt_{0.7}Ru_{0.3}$, $Pt_{0.6}Ru_{0.4}$, and $Pt_{0.5}Ru_{0.5}$. (c) Adsorption energies of CO and OH on the surfaces of $Pt_{0.7}Ru_{0.3}$, $Pt_{0.6}Ru_{0.4}$, and $Pt_{0.5}Ru_{0.5}$. (d) Differential charge density distributions of OH adsorbed on the surfaces of $Pt_{0.7}Ru_{0.3}$, $Pt_{0.6}Ru_{0.4}$, and $Pt_{0.5}Ru_{0.5}$. (e, f) Projected density of states (PDOS) of CO and OH adsorbed on the surfaces of $Pt_{0.7}Ru_{0.3}$, $Pt_{0.6}Ru_{0.4}$, and $Pt_{0.5}Ru_{0.5}$. (g) MOR free energy profiles for $Pt_{0.7}Ru_{0.3}$, $Pt_{0.6}Ru_{0.4}$, and $Pt_{0.5}Ru_{0.5}$.

performance catalysts show strong OH and weak CO adsorption.[25] $Pt_{0.6}Ru_{0.4}$ has the weakest CO and strongest OH adsorption (Figures 4c and S23), reducing CO poisoning and promoting intermediate transformation. Charge density difference and Bader charge analysis support this, with $Pt_{0.6}Ru_{0.4}$ showing the strongest OH charge transfer and weakest CO charge transfer (Figures 4d and S24−S26). Figure 4e,f compares the projected density of states (PDOS) of OH and CO adsorption on $Pt_{0.7}Ru_{0.3}$, $Pt_{0.6}Ru_{0.4}$, and $Pt_{0.5}Ru_{0.5}$. The *d*-band center relative to the Fermi level (E_F) reflects intermediate adsorption strength and electronic structure.[26] $Pt_{0.6}Ru_{0.4}$ has the highest *d*-band center after OH adsorption, enhancing Ru−O bonding. Crystal orbital Hamilton population (COHP) analysis confirms this, with $Pt_{0.6}Ru_{0.4}$ showing the highest negative integrated COHP value (Figure S27). After CO adsorption, $Pt_{0.6}Ru_{0.4}$ has the lowest *d*-band center, facilitating *CO removal through synergistic oxidation. The transition state energy barrier for the rate-determining step (*CHO + *OH → *HCOOH)[27] is lowest for $Pt_{0.6}Ru_{0.4}$, indicating superior reaction kinetics (Figures 4g and S28), consistent with results in Figure 4a. DFT calculations highlight the importance of optimizing the Pt−Ru alloy ratio for enhancing MOR activity.

Our work introduces a novel strategy that merges ultrafast precision synthesis and ultrasonic exfoliation to create colloidal Pt_xRu_{1-x} catalysts with tunable compositions, exceptional monodispersity, and near-pristine surfaces. This approach overcomes a long-standing challenge in the synthesis of colloidal NPs for single NP collision electrocatalysis. Traditional methods often rely on long-chain stabilizers that obscure active sites, limiting their application. In contrast, our method produces NPs with tunable compositions and uniform sizes while maximizing the availability of active sites. This innovation enables the study of catalytic behavior at the single NP level, providing unprecedented insights into the intrinsic activity of MOR at industrial current densities, bypassing mass transfer limitations. The integration of single NP collision electrocatalysis with DFT calculations further reveals the Pt−Ru synergistic effects in optimizing MOR performance, highlighting the importance of alloy composition in enhancing catalytic activity.

This study demonstrates a new paradigm for identifying advanced multicomponent electrocatalysts by combining ultrafast precision synthesis with single NP collision electrocatalysis. The ability to rapidly screen catalysts with different compositions significantly accelerates the discovery process, offering valuable insights for the design of next-generation electrocatalysts with enhanced performance. Our findings not only address critical challenges in colloidal catalyst synthesis but also provide a comprehensive framework for understanding the relationship between composition and activity at the single NP level, as well as the underlying mechanisms.

ASSOCIATED CONTENT

Supporting Information

The Supporting Information is available free of charge at https://pubs.acs.org/doi/10.1021/acs.nanolett.5c01519.

Experimental sections and additional characterization data, including Figures S1−S28 and Tables S1−S5 (PDF)

AUTHOR INFORMATION

Corresponding Author

Min Zhou − *State Key Laboratory of Electroanalytical Chemistry, Changchun Institute of Applied Chemistry, Chinese Academy of Sciences, Changchun 130022, China; School of Applied Chemistry and Engineering, University of Science and Technology of China, Hefei 230026, China;* orcid.org/0000-0003-4073-5370; Email: mzhou1982@ciac.ac.cn

Authors

Lixia Yang − *State Key Laboratory of Electroanalytical Chemistry, Changchun Institute of Applied Chemistry, Chinese Academy of Sciences, Changchun 130022, China; School of Applied Chemistry and Engineering, University of Science and Technology of China, Hefei 230026, China*

Yuanhua Tu − *Guangdong Provincial Key Laboratory of Fuel Cell Technology, School of Chemistry and Chemical Engineering, South China University of Technology, Guangzhou 510641, China*

Xiangyi Shan − *State Key Laboratory of Electroanalytical Chemistry, Changchun Institute of Applied Chemistry, Chinese Academy of Sciences, Changchun 130022, China; School of Applied Chemistry and Engineering, University of Science and Technology of China, Hefei 230026, China;* orcid.org/0009-0005-2536-2491

Pengfei Wang − *Institute of Fundamental and Frontier Sciences, University of Electronic Science and Technology of China, Sichuan, Chengdu 610054, China*

Jianan Xu − *State Key Laboratory of Electroanalytical Chemistry, Changchun Institute of Applied Chemistry, Chinese Academy of Sciences, Changchun 130022, China;* orcid.org/0009-0000-5649-9275

Han Gao − *State Key Laboratory of Electroanalytical Chemistry, Changchun Institute of Applied Chemistry, Chinese Academy of Sciences, Changchun 130022, China*

Furong Cai − *State Key Laboratory of Electroanalytical Chemistry, Changchun Institute of Applied Chemistry, Chinese Academy of Sciences, Changchun 130022, China*

Zhiming Cui − *Guangdong Provincial Key Laboratory of Fuel Cell Technology, School of Chemistry and Chemical Engineering, South China University of Technology, Guangzhou 510641, China;* orcid.org/0000-0002-0305-4181

Zhaoyu Jin − *Institute of Fundamental and Frontier Sciences, University of Electronic Science and Technology of China, Sichuan, Chengdu 610054, China;* orcid.org/0000-0003-0840-3931

Complete contact information is available at: https://pubs.acs.org/10.1021/acs.nanolett.5c01519

Author Contributions

M.Z. conceived and supervised the project. L.Y. performed the experiments, analyzed the data, and wrote the initial draft. Y.T. carried out the DFT calculations. P.W. created the illustration for the manuscript. X.S., J.X., H.G., F.C., Z.C., and Z.J. assisted with the writing and revision of the manuscript. All the authors participated in the writing of the paper.

Notes

The authors declare no competing financial interest.

ACKNOWLEDGMENTS

This work was supported by National Natural Science Foundation of China (22204159, 22304021) and the Major Project of Changchun State Key Laboratory (23GZZ05).

REFERENCES

(1) Yao, Y.; Dong, Q.; Brozena, A.; Luo, J.; Miao, J.; Chi, M.; Wang, C.; Kevrekidis, I. G.; Ren, Z. J.; Greeley, J.; Wang, G.; Anapolsky, A.; Hu, L. High-entropy nanoparticles: Synthesis-structure-property relationships and data-driven discovery. *Science* **2022**, *376* (6589), No. eabn3103.

(2) Xiao, X.; Bard, A. J. Observing Single Nanoparticle Collisions at an Ultramicroelectrode by Electrocatalytic Amplification. *J. Am. Chem. Soc.* **2007**, *129* (31), 9610−9612.

(3) Lu, S.-M.; Chen, M.; Wen, H.; Zhong, C.-B.; Wang, H.-W.; Yu, Z.; Long, Y.-T. Hydrodynamics-Controlled Single-Particle Electrocatalysis. *J. Am. Chem. Soc.* **2024**, *146* (22), 15053−15060.

(4) Lu, S. M.; Wang, H. W.; Chen, M.; Xie, B. K.; Long, Y. T. Unlocking Single Particle Anisotropy in Real-Time for Photoelectrochemistry Processes at the Nanoscale. *Angew. Chem., Int. Ed.* **2024**, *136* (32), No. e202404170.

(5) Li, H.; Zhang, X.; Sun, Z.; Ma, W. Rapid Screening of Bimetallic Electrocatalysts Using Single Nanoparticle Collision Electrochemistry. *J. Am. Chem. Soc.* **2022**, *144* (36), 16480−16489.

(6) Sun, Z.; Wang, J.; Su, L.; Gu, Z.; Wu, X.-P.; Chen, W.; Ma, W. Dynamic Evolution and Reversibility of a Single Au25 Nanocluster for the Oxygen Reduction Reaction. *J. Am. Chem. Soc.* **2024**, *146* (29), 20059−20068.

(7) Vannoy, K. J.; Lee, I.; Sode, K.; Dick, J. E. Electrochemical quantification of accelerated FADGDH rates in aqueous nanodroplets. *Proc. Natl. Acad. Sci. U. S. A.* **2021**, *118* (25), No. e2025726118.

(8) Quast, T.; Aiyappa, H. B.; Saddeler, S.; Wilde, P.; Chen, Y.-T.; Schulz, S.; Schuhmann, W. Single-Entity Electrocatalysis of Individual “Picked-and-Dropped” Co_3O_4 Nanoparticles on the Tip of a Carbon Nanoelectrode. *Angew. Chem., Int. Ed.* **2021**, *60* (7), 3576−3580.

(9) Quast, T.; Varhade, S.; Saddeler, S.; Chen, Y.-T.; Andronescu, C.; Schulz, S.; Schuhmann, W. Single Particle Nanoelectrochemistry Reveals the Catalytic Oxygen Evolution Reaction Activity of Co_3O_4 Nanocubes. *Angew. Chem., Int. Ed.* **2021**, *60* (43), 23444−23450.

(10) Lv, X.; Tian, Y.; Wu, F.; Luan, X.; Li, F.; Shen, Z.; Xu, G.; Liu, K.; Niu, W. Chiral plasmonic-dielectric coupling enables strong near-infrared chiroptical responses from helicoidal core-shell nanoparticles. *Nat. Commun.* **2024**, *15* (1), 9234.

(11) Crawley, J. W. M.; Gow, I. E.; Lawes, N.; Kowalec, I.; Kabalan, L.; Catlow, C. R. A.; Logsdail, A. J.; Taylor, S. H.; Dummer, N. F.; Hutchings, G. J. Heterogeneous trimetallic nanoparticles as catalysts. *Chem. Rev.* **2022**, *122* (6), 6795−6849.

(12) Clarke, T. B.; Krushinski, L. E.; Vannoy, K. J.; Colón-Quintana, G.; Roy, K.; Rana, A.; Renault, C.; Hill, M. L.; Dick, J. E. Single entity electrocatalysis. *Chem. Rev.* **2024**, *124* (15), 9015−9080.

(13) Zhong, R.; Wang, X.; Tao, Q.; Zhang, J.; Lin, C.; Wei, H.; Zhou, Y. G. From ensemble electrochemistry to nano-impact electrochemistry: altered reaction selectivity. *Angew. Chem., Int. Ed.* **2022**, *61* (37), No. e202207270.

(14) Park, J.-W.; Shumaker-Parry, J. S. Structural study of citrate layers on gold nanoparticles: role of intermolecular interactions in stabilizing nanoparticles. *J. Am. Chem. Soc.* **2014**, *136* (5), 1907−1921.

(15) Liang, J.; Cao, G.; Zeng, M.; Fu, L. Controllable synthesis of high-entropy alloys. *Chem. Soc. Rev.* **2024**, *53*, 6021−6041.

(16) Cui, M.; Yang, C.; Hwang, S.; Yang, M.; Overa, S.; Dong, Q.; Yao, Y.; Brozena, A. H.; Cullen, D. A.; Chi, M.; Blum, T. F.; et al. Multi-principal elemental intermetallic nanoparticles synthesized via a disorder-to-order transition. *Sci. Adv.* **2022**, *8* (4), No. eabm4322.

(17) Pan, Y.; Shan, X.; Cai, F.; Gao, H.; Xu, J.; Zhou, M. Accelerating the Discovery of Oxygen Reduction Electrocatalysts: High-Throughput Screening of Element Combinations in Pt-Based High-Entropy Alloys. *Angew. Chem., Int. Ed.* **2024**, *63* (37), No. e202407116.

(18) Shan, X.; Pan, Y.; Cai, F.; Gao, H.; Xu, J.; Liu, D.; Zhu, Q.; Li, P.; Jin, Z.; Jiang, J.; Zhou, M. Accelerating the Discovery of Efficient High-Entropy Alloy Electrocatalysts: High-Throughput Experimentation and Data-Driven Strategies. *Nano Lett.* **2024**, *24* (37), 11632−11640.

(19) Mariano, R. G.; Kang, M.; Wahab, O. J.; McPherson, I. J.; Rabinowitz, J. A.; Unwin, P. R.; Kanan, M. W. Microstructural origin of locally enhanced CO_2 electroreduction activity on gold. *Nat. Mater.* **2021**, *20* (7), 1000−1006.

(20) Wahab, O.; Daviddi, E.; Xin, B.; Sun, P.; Griffin, E.; Colburn, A.; Barry, D.; Yagmurcukardes, M.; Peeters, F.; Geim, A.; Lozada-Hidalgo, M.; Unwin, P. R. Proton transport through nanoscale corrugations in two-dimensional crystals. *Nature* **2023**, *620* (7975), 782−786.

(21) Lu, S.-M.; Chen, J.-F.; Peng, Y.-Y.; Ma, W.; Ma, H.; Wang, H.-F.; Hu, P.; Long, Y.-T. Understanding the Dynamic Potential Distribution at the Electrode Interface by Stochastic Collision Electrochemistry. *J. Am. Chem. Soc.* **2021**, *143* (32), 12428−12432.

(22) Gao, H.; Xu, J.; Zhang, X.; Zhou, M. Benchmarking the Intrinsic Activity of Transition Metal Oxides for the Oxygen Evolution Reaction with Advanced Nanoelectrodes. *Angew. Chem., Int. Ed.* **2024**, *63*, No. e202404663.

(23) Liu, C.; Xu, J.; Gao, H.; Zhou, M.; Lu, L. Nitrogen-skinned carbon nanocone enables non-dynamic electrochemistry of individual metal particles. *Sci. China Chem.* **2022**, *65* (10), 2031−2037.

(24) Zhou, Y. G.; Rees, N. V.; Compton, R. G. The electrochemical detection and characterization of silver nanoparticles in aqueous solution. *Angew. Chem., Int. Ed.* **2011**, *18* (50), 4219−4221.

(25) Zhang, Z.; Liu, J.; Wang, J.; Wang, Q.; Wang, Y.; Wang, K.; Wang, Z.; Gu, M.; Tang, Z.; Lim, J.; et al. Single-atom catalyst for high-performance methanol oxidation. *Nat. Commun.* **2021**, *12* (1), 5235.

(26) Tian, J.; Rao, Y.; Shi, W.; Yang, J.; Ning, W.; Li, H.; Yao, Y.; Zhou, H.; Guo, S. Sabatier Relations in Electrocatalysts Based on High-entropy Alloys with Wide-distributed d-band Centers for Li-O_2 Batteries. *Angew. Chem., Int. Ed.* **2023**, *62* (44), No. e202310894.

(27) Huang, L.; Zhang, X.; Wang, Q.; Han, Y.; Fang, Y.; Dong, S. Shape-control of Pt-Ru nanocrystals: tuning surface structure for enhanced electrocatalytic methanol oxidation. *J. Am. Chem. Soc.* **2018**, *140* (3), 1142−1147.